

## Use of In-situ Thermography to Study Scan Strategy for Laser Foil Printing of Metallic Glass

Hung-Chu Chiang, Sung-Heng Wu, Chia-Hung Hung, Ming C. Leu

Department of Mechanical and Aerospace Engineering, Missouri University of  
Science and Technology, Rolla, MO, United States.

Department of Mechanical Engineering, National Cheng Kung University, Tainan,  
Taiwan.

### Abstract

This study investigates the Laser-Foil-Printing (LFP) additive manufacturing process to fabricate zirconium-based metallic glass ( $Zr_{65.7}Cu_{15.6}Ni_{11.7}Al_{3.7}Ti_{3.3}$ ) samples, by utilizing in-situ thermography to obtain the relationship between laser scanning strategy and melt-pool cooling rates. To monitor thermal behavior during LFP processing, a mid-wavelength infrared (MWIR) camera was used to capture the temperature data of melt pool and heat-affected zone in real time. This research focuses on cooling rates and temperature evolution required for maintaining amorphous structure and avoiding crystallization. Both continuous welding and discrete welding strategies were evaluated. Continuous welding produces a broader heat-affected zone with gradually decreasing cooling rates, while discrete welding generates localized heat input with higher and more stable cooling rates at individual weld spot locations. The experimental results highlight the critical role of laser scan strategy and thermal dynamics in controlling microstructure and quality of LFP-fabricated metallic glass.

### Keywords

Additive Manufacturing, Metallic Glass, Laser-Foil-Printing, In-situ Thermal Graphic Monitoring

## 1. Introduction

Metallic glasses (MGs), known for their high strength, hardness, excellent corrosion resistance, and favorable magnetic properties, have been widely applied in aerospace, biomedical, and electronic industries. However, forming and maintaining an amorphous structure requires extremely high cooling rates, which poses a significant challenge for traditional manufacturing methods. The rapid heating and cooling cycles inherent to additive manufacturing, particularly laser-based methods, combined with its

layer-by-layer fabrication nature, make it possible to produce bulk metallic glass (BMG) alloys [1].

Among various additive manufacturing (AM) techniques, laser powder bed fusion (LPBF) has been applied in fabricating Zr-based metallic glasses. Although LPBF enables the direct construction of complex geometries from metal powders, studies have shown that the process often results in partial crystallization and heterogeneous microstructures due to insufficient cooling rates and repeated thermal cycling. For instance, crystalline phases embedded within the amorphous matrix have been observed in  $Zr_{57}Cu_{15}Ni_{10}Nb_5$  alloys fabricated by LPBF, significantly affecting their mechanical properties [2].

Laser foil printing (LFP) has recently emerged as a promising alternative for metal additive manufacturing. LFP fabricates parts by stacking and selectively melting metal foils layer by layer, offering the advantage of complex geometry fabrication with reduced material waste [3], while also exhibiting excellent mechanical properties [4]. However, metallic glasses (MGs), or amorphous metals, are highly sensitive to thermal history. Without sufficient cooling rates and precise thermal control during processing, localized crystallization, thermal accumulation, and structural defects can easily occur, compromising the stability of the amorphous phase and the overall performance of the fabricated parts [5-7].

A key limitation of the current LFP system is the lack of real-time thermal monitoring, making it difficult to effectively control melt pool temperature and cooling behavior, which hinders process optimization and quality assurance [8]. While some studies have introduced in-situ thermal imaging into LFP using stainless steel substrates such as SS304 [9], applications to metallic glass systems remain scarce. Given the extreme sensitivity of MGs to thermal variations, precise thermal monitoring during fabrication is even more critical.

This study introduces mid-wavelength infrared (MWIR) thermographic imaging as an in-situ monitoring method for the LFP process of metallic glasses. By capturing high-resolution spatiotemporal thermal data, this technique enables direct observation of melt pool dynamics and heat-affected zone (HAZ) distributions, providing critical insight into cooling performance and crystallization risks. A comparative analysis is conducted between two laser scanning strategies—continuous welding and discrete welding—by integrating MWIR thermography with X-ray diffraction (XRD) and microhardness testing. The results reveal how different scanning strategies influence

cooling behavior, interlayer heat accumulation, and amorphous structure retention. These findings provide a basis for optimizing LFP process parameters and improving the reliability and scalability of MG additive manufacturing.

## 2. Experimental Setup

### 2-1. LFP System

In the LFP process, two types of lasers were employed for layer-by-layer foil fabrication: a continuous-wave (CW) fiber laser (IPG YLR-1000) for welding and a pulsed ultraviolet (UV) laser (Coherent AVIA-355X) for cutting. The CW fiber laser was used in both spot welding and patterned welding operations. It was integrated with a SCANLAB HurrySCAN 20 galvanometer scanning system and a 330 mm F-theta lens, resulting in a focused beam spot size of 0.16 mm and a beam quality ( $M^2$ ) of 3.04. For precision contour cutting, the Coherent AVIA-355X UV pulsed laser was employed. It provides a maximum output of 10 W at a pulse repetition rate of 100 kHz and is equipped with a 100 mm focal length lens that achieves a fine 0.04 mm spot size.

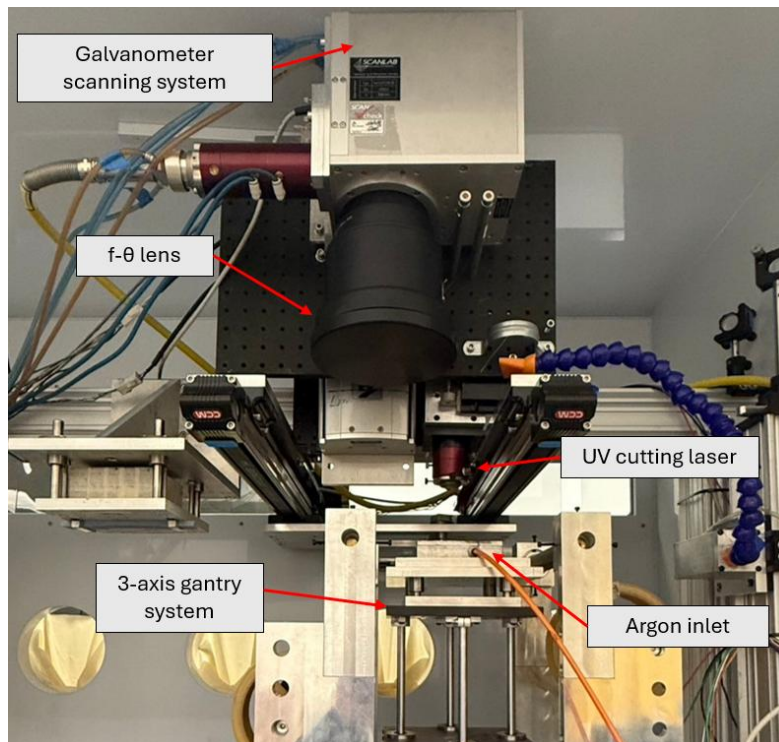


Figure 1. Photo of the in-house developed LFP system.

In the Laser Foil Printing (LFP) process, a laser beam selectively melts metal foil to fabricate components with defined geometries and patterns. As illustrated in Figure 2, the process consists of four steps for each layer: (a) spot welding, (b) pattern welding, (c) contour cutting, and (d) surface polishing. All operations were conducted in an argon-filled chamber to minimize oxidation.

The first step, spot welding, is designed to securely bond the incoming metal foil to the substrate or the previously deposited layer. A pressure plate with laser-permeable holes clamps the foil in place, while a spring-loaded mechanism ensures firm contact with the underlying surface. This step is crucial for reducing thermal distortion during subsequent processing. The second step, pattern welding, is the core of the LFP process. Here, the laser beam selectively melts the foil according to the programmed geometry, enabling layer-by-layer fabrication of the target structure. Following this, contour cutting is performed to remove excess foil and define the part's outer boundary. This step may generate burrs along the cut edges, which can compromise the quality of the next weld layer.

To address this issue, surface polishing is carried out as the final step. Mechanical polishing using a grindstone is applied to remove burrs and flatten the surface, thereby ensuring suitable conditions for subsequent foil deposition and welding.

Post-process characterization included microstructural analysis using X-ray diffraction (XRD, Philips X'pert MPD) on a  $1 \times 1 \text{ mm}^2$  surface area. Additionally, metallographic specimens were prepared via sawing, mounting, and polishing. Vickers microhardness measurements were conducted using a Struers Duramin 5 tester under a 490.6 mN load with a 10 s load duration.

In the experimental setup, a zirconium-based metallic glass foil (LM105,  $\text{Zr}_{65.7}\text{Cu}_{15.6}\text{Ni}_{11.7}\text{Al}_{3.7}\text{Ti}_{3.3}$ ) with a thickness of 0.1 mm was utilized as the feedstock material. To enhance fabrication efficiency and build rate, two sheets of foil were stacked to form a single layer, resulting in a total thickness of approximately 0.2 mm per deposited layer. The substrate was a Zr702 alloy block with dimensions of 40 mm  $\times$  40 mm  $\times$  5 mm.

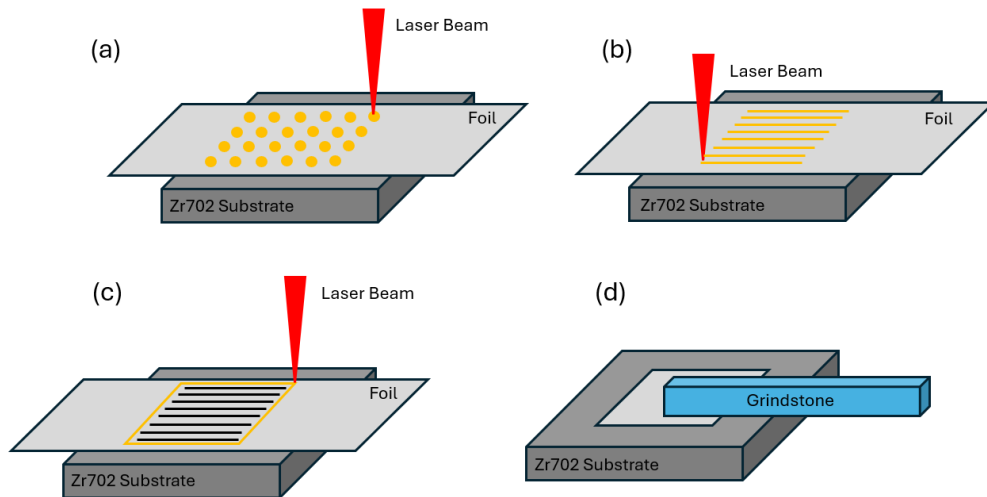


Figure 2. LFP process steps: (a) spot welding, (b) pattern welding, (c) contour cutting, and (d) surface polishing.

Two laser scanning strategies—continuous welding and discrete welding—were investigated. For both scanning strategies, the laser power ( $P$ ) was maintained at 500 W and the scan speed ( $v$ ) at 500 mm/s. To mitigate heat accumulation and prevent remelting, a 10 s delay was introduced between successive scan lines in continuous welding, while a 125 ms interval was applied between adjacent points in discrete welding.

## 2-2. Monitoring

To facilitate real-time monitoring of melt pool temperature distribution, a Telops FAST M3K mid-wavelength infrared (MWIR) camera (Model TEL-11340) was employed. This camera operates in the 3–5.5  $\mu\text{m}$  spectral range and is equipped with an  $f/2.5$  Indium Antimonide (InSb) detector, coupled with a G1X microscope lens (Model TEL-10032). The system supports high-speed imaging, capable of reaching a maximum frame rate of 100 kHz.

Figure 3 presents the experimental setup. A high-speed infrared (IR) camera was positioned outside the argon-filled chamber, mounted on a tripod and aligned with a barium fluoride ( $\text{BaF}_2$ ) window installed on the chamber wall. This window permits mid-wavelength infrared transmission, allowing the camera to directly capture thermal emissions from the melt pool during laser processing.

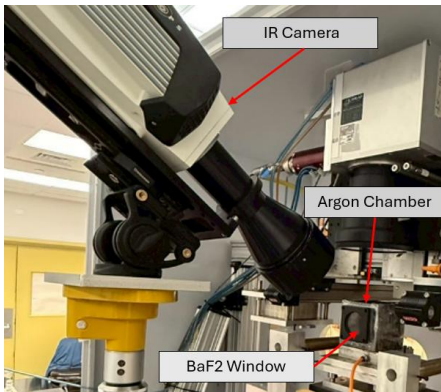


Figure 3. Photo of the IR camera during in-situ process monitoring.

Prior to data acquisition, a series of preliminary trials were conducted to optimize critical imaging parameters, including spatial resolution, frame rate, and exposure time. These parameters are interdependent and collectively influence the accuracy and quality of thermal measurements.

Exposure time was found to be a key determinant of image quality. Overexposure may lead to pixel saturation in high-temperature regions, while underexposure results in a poor signal-to-noise ratio. After systematic evaluation, an exposure time of 5  $\mu$ s was determined to provide the optimal balance, ensuring accurate thermal data capture for both continuous and discrete welding processes.

As summarized in Table 1, calibration blocks of Telops camera were selected to encompass the temperature range relevant to melting and solidification phenomena. Given the study's focus on these dynamic thermal processes, filter wheel 3 was chosen for data acquisition. Although this filter sets a minimum detectable temperature at 365  $^{\circ}$ C, it is well-suited for capturing melt pool evolution and estimating cooling rates.

For thermal analysis, thirty representative points were extracted along each laser scan path, as shown in Figure 4. This point-based sampling strategy was consistently applied across both scanning conditions to allow direct comparison of temperature histories and cooling behaviors. The 30 points were evenly spaced along the scan direction to capture transient thermal responses, including variations in peak temperature, melting duration, and cooling rate. This approach enabled a detailed investigation into the influence of scanning strategy on localized thermal dynamics and interlayer heat accumulation.

Table 1. Filter wheel configurations for calibration blocks of the Telops camera.

Filter Wheel	Spectral Range	Temperature Range
1	3.08 $\mu\text{s}$ – 5.41 $\mu\text{s}$	0 °C – 194 °C
2	3.08 $\mu\text{s}$ – 5.41 $\mu\text{s}$	173 °C – 533 °C
3	3.08 $\mu\text{s}$ – 5.41 $\mu\text{s}$	365 °C – 1230 °C
4	3.08 $\mu\text{s}$ – 5.41 $\mu\text{s}$	819 °C – 2500 °C

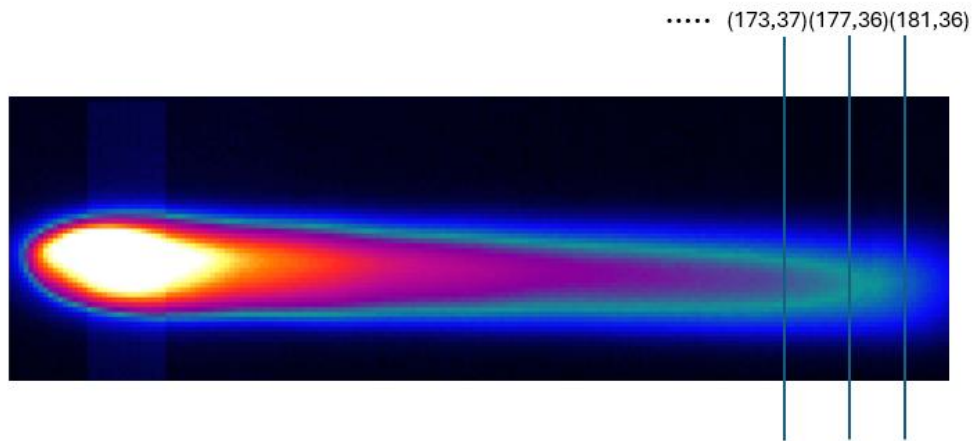


Figure 4. Points of laser scan path with respect to pixel coordinates.

### 3. Results and discussion

#### 3-1. Temperature History

To further investigate the thermal behavior for the two laser welding strategies, this study analyzed the temperature histories of the third and fourth layers for both continuous and discrete welding.

In continuous welding, all measurement points exhibited a sharp temperature rise to approximately 1100–1150 K, followed by rapid cooling to a stable baseline, as shown in Figures 5 and 7. This indicates strong thermal concentration due to the continuous input of laser energy. Further analysis reveals that most points remained above the melting point of LM105 (~1070 K) for only a brief period, suggesting that the molten regions were highly localized and transient. However, many points stayed within the crystallization temperature range (~720–750 K) for an extended duration, potentially increasing the risk of localized crystallization.

In the third layer (C3), a steep temperature gradient near the melt pool boundary facilitated effective heat dissipation. In contrast, the fourth layer (C4) showed slower temperature decay and higher final temperatures (~ 530–550 K), which were higher than those in C3. This suggests significant heat accumulation from the previous layers, resulting in weakened thermal gradients. Although C3 and C4 exhibited similar peak temperatures, their thermal histories differed substantially: C3 had faster cooling and less residual heat, favoring the stability of the amorphous phase, whereas C4 demonstrated greater thermal retention, raising the risk of crystallization.

To analyze the thermal behavior during continuous welding, temperature histories were compared at the start point and midpoint of the laser scan, as shown in Figures 6(a), (b) and 8(a), (b). The results show that the start point exhibits a rapid temperature drop and the steepest gradient, indicating rapid solidification. The midpoint shows a more gradual decline, possibly influenced by prior heat accumulation, reflecting overall heat buildup. The overall trend indicates that the rate of temperature decay gradually decreases along the scanning direction.

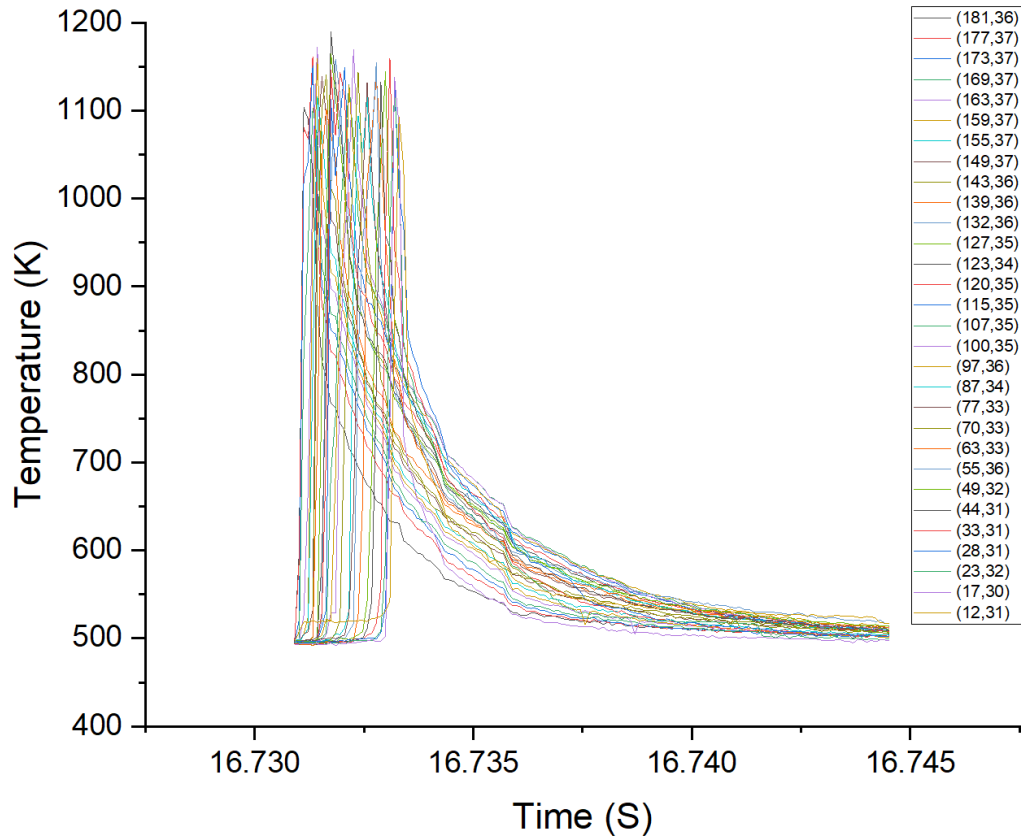


Figure 5. Temperature results of IR recording for the continuous scanning strategy in the third layer.

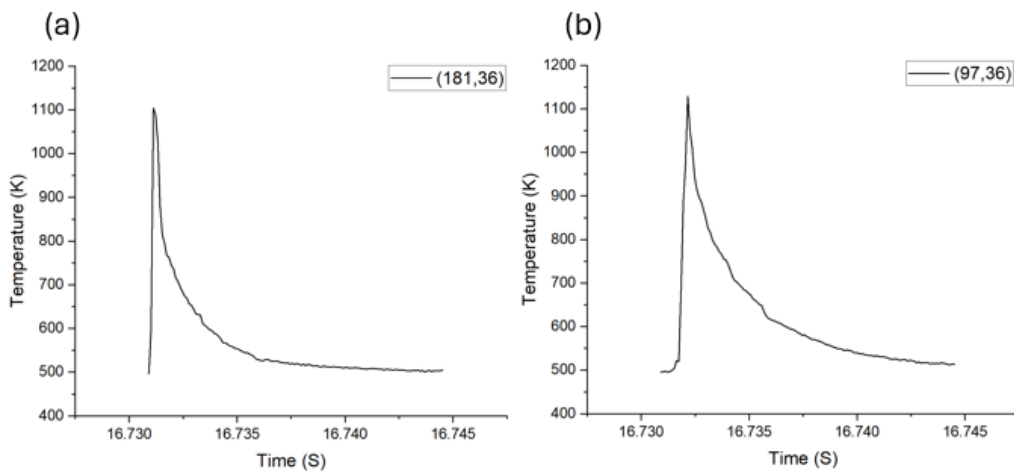


Figure 6. Temperature results of IR recording for the continuous scanning strategy in the third layer: (a) start point, (b) midpoint.

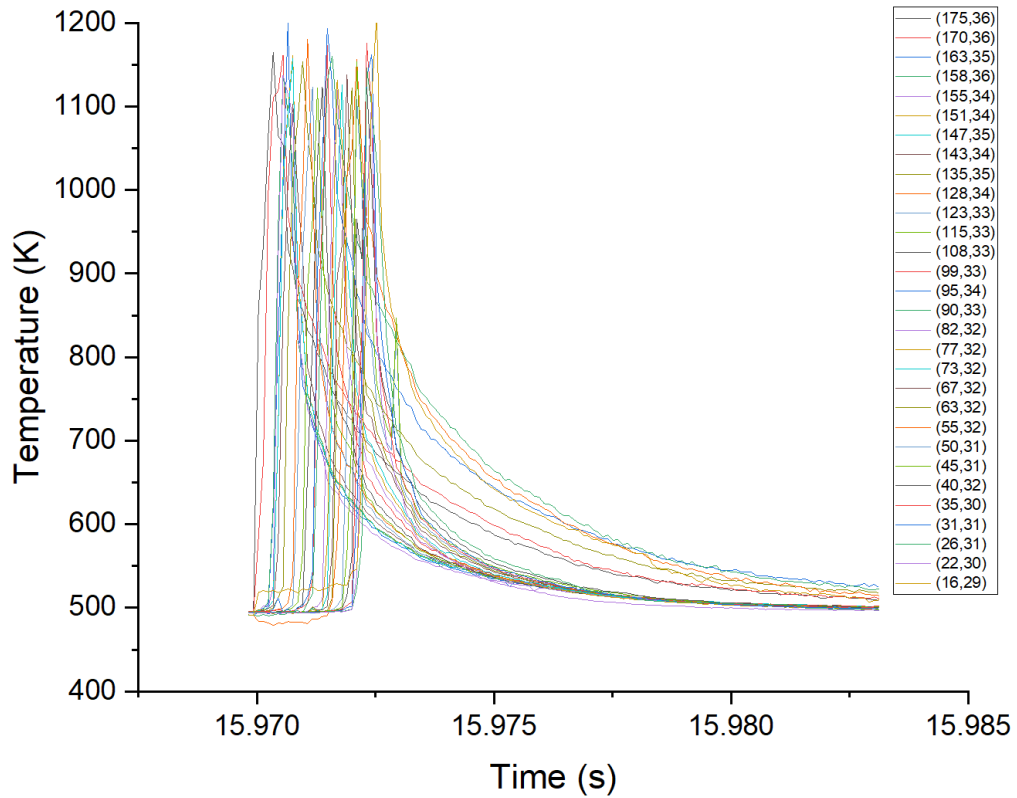


Figure 7. Temperature results of IR recording for the continuous scanning strategy in the fourth layer.

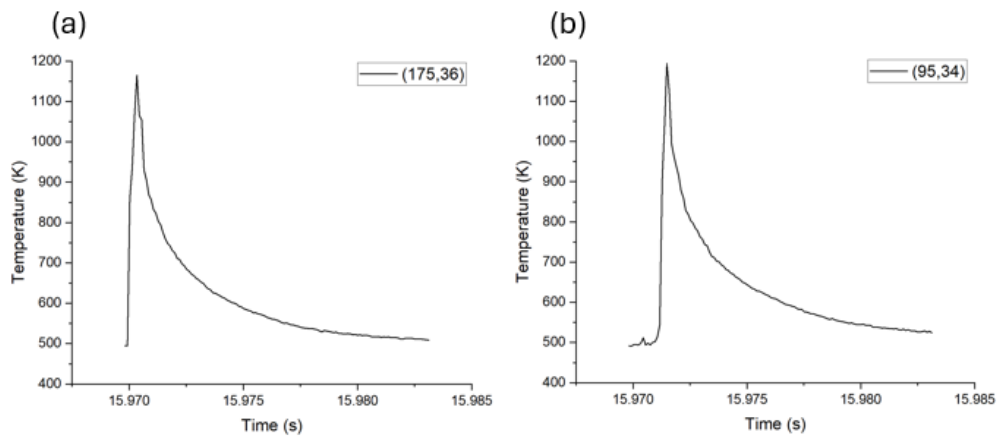


Figure 8. Temperature results of IR recording for the continuous scanning strategy in the fourth layer: (a) start point, (b) midpoint.

In contrast, under discrete welding conditions, the third (D3) and fourth (D4) layers exhibited multiple periodic thermal spikes, with each laser pulse rapidly heating the material to 1100–1150 K, followed by swift cooling back to ~500 K, as shown in Figures 9 and 10. These sharp peaks correspond to individual laser spots, highlighting the highly localized thermal input characteristic of the discrete scanning strategy. Each melting event lasted for an extremely short time. Although the crystallization temperature range was repeatedly reached, the duration of exposure was short enough to maintain favorable conditions for amorphous structure formation.

Furthermore, the temperature histories of D3 and D4 were nearly identical, indicating minimal interlayer heat accumulation. The discrete strategy provided repeatable, well-separated thermal cycles with strong spatial thermal gradients, which helped maintain thermal stability across layers. Due to the highly localized and intermittent nature of the heat input, the extent of the heat-affected zone (HAZ) was significantly reduced, effectively avoiding structural changes in adjacent regions.

The temperature profiles also allow estimation of the HAZ. In continuous welding, the sustained laser input caused the surrounding material to remain at high temperatures for prolonged periods—especially within the crystallization range (~720–750 K), leading to a significantly expanded HAZ. This not only increases the risk of crystallization but may also degrade mechanical properties. In contrast, discrete welding involved highly localized and short-duration heat input with sufficient cooling intervals. As a result, heat was less likely to spread to adjacent areas, and the HAZ was confined to a very small region near the melt pool. This behavior is beneficial for preserving the amorphous structure and mechanical stability of the surrounding material.

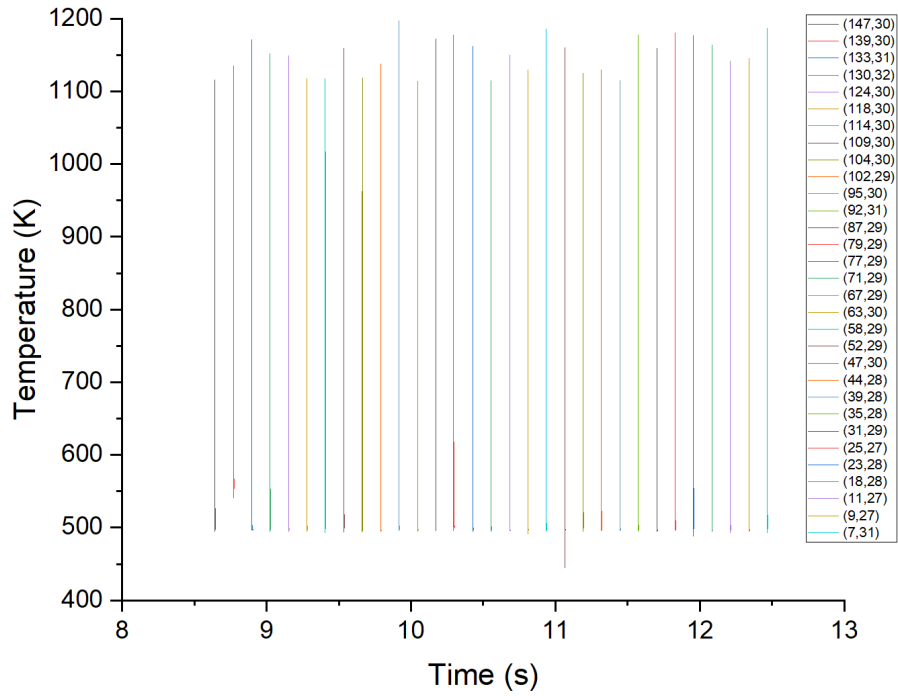


Figure 9. Temperature results of IR recording for the discrete scanning strategy in the third layer.

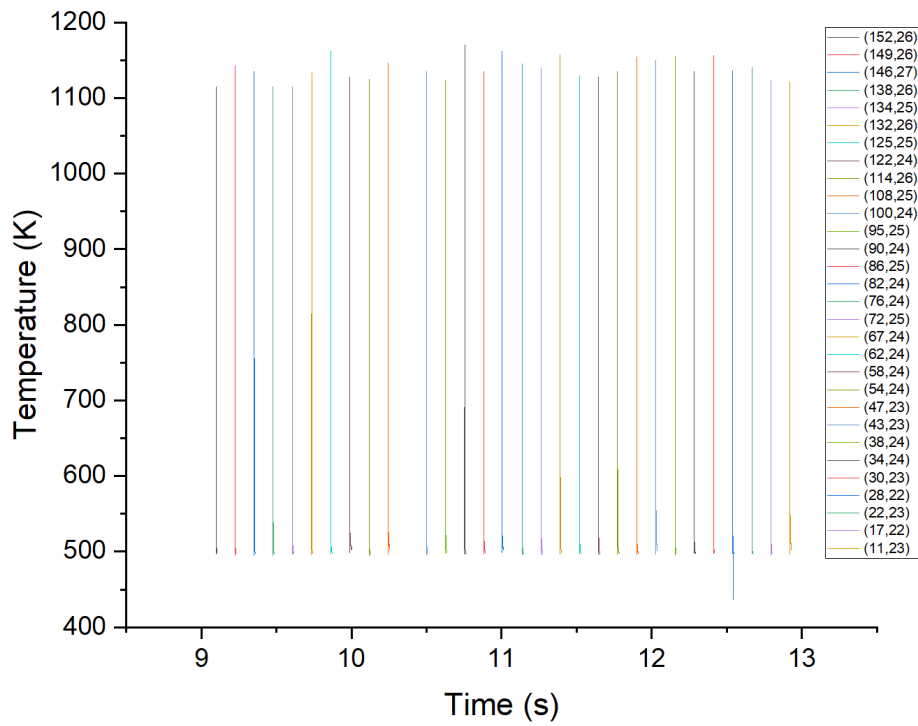


Figure 10. Temperature results of IR recording for the discrete scanning strategy in the fourth layer.

In summary, continuous welding results in prolonged and cumulative heating, which can lead to interlayer heat buildup, particularly in upper layers, thereby expanding the HAZ and increasing the risk of crystallization. In contrast, discrete welding maintains steeper thermal gradients, minimizes heat accumulation, enhances cooling efficiency, and significantly reduces the HAZ, demonstrating superior thermal control capability.

### **3-2. Cooling Rate**

To investigate the effects of different laser scanning strategies on cooling behavior, this study analyzed the cooling rates of the third and fourth layers under continuous and discrete welding conditions. In this study, the cooling rate is obtained by calculating temperature change over time ( $\Delta T / \Delta t$ ), where positive values represent cooling (temperature drop) and negative values represent heating (temperature rise). The two scanning strategies exhibit distinct differences in cooling behavior, including peak cooling rate, temporal distribution, spatial thermal gradients, intra-layer variation trends, and interlayer heat accumulation.

In continuous welding, a sharp positive cooling peak is generated immediately after laser exposure, with a maximum rate reaching up to  $5.74 \times 10^6$  K/s, followed by a rapid return of temperature to near zero, reflecting instantaneous energy input and rapid heat dissipation, as shown in Figures 11 and 13. However, a closer examination of cooling rate variations at different positions within the same layer reveals a gradual decrease in cooling rate along the scanning path, which is particularly evident in C4. This phenomenon reflects thermal accumulation from the previous layers, leading to an elevated local substrate temperature, which reduces the temperature difference between the melt pool and the surrounding environment, indicated a reduction in thermal gradient, ultimately decreasing the cooling rate. In contrast, C3 exhibits a steeper initial thermal gradient, which promotes more efficient heat dissipation, resulting in relatively higher cooling rates.

The cooling rate analysis further reveals the thermal behavior variation along the scanning direction during the continuous welding process. Cooling rates were compared at the start point and midpoint of the laser scan, as shown in Figures 12(a), (b) and 14(a), (b). The start point exhibits the highest cooling rate peak with a stable curve and minimal fluctuation, indicating localized and efficient heat dissipation. In the middle section, the cooling rate is slightly lower with mild oscillations, likely due to a combination of localized heat accumulation and thermal diffusion. This trend confirms

that cooling efficiency gradually deteriorates along the scanning direction during the laser processing.

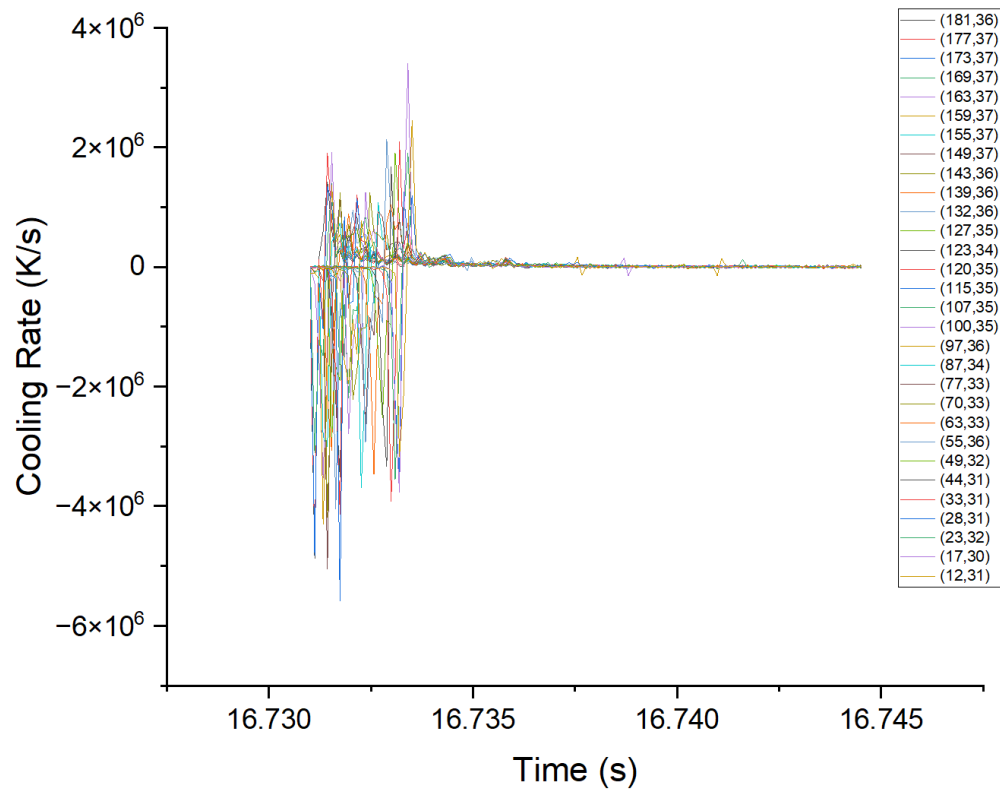


Figure 11. Cooling rate results of IR recording for the continuous scanning strategy in the third layer.

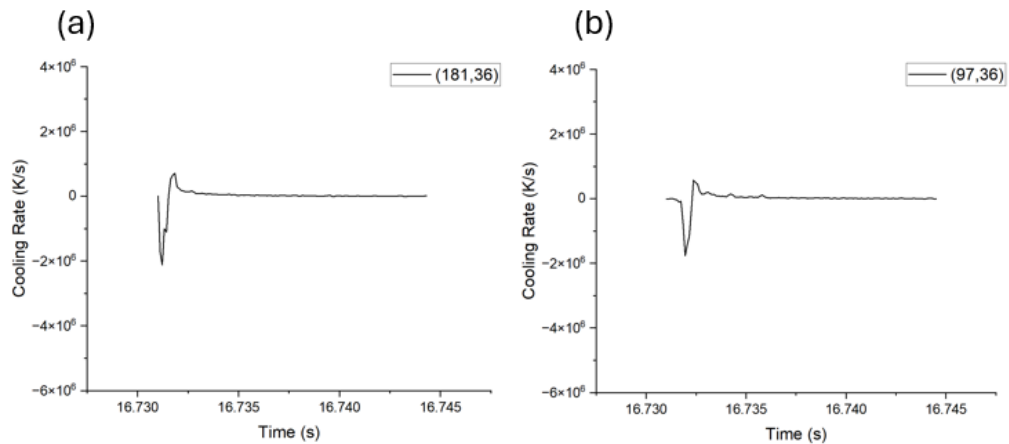


Figure 12. Cooling rate results of IR recording for the continuous scanning strategy in the third layer: (a) start point, (b) midpoint.

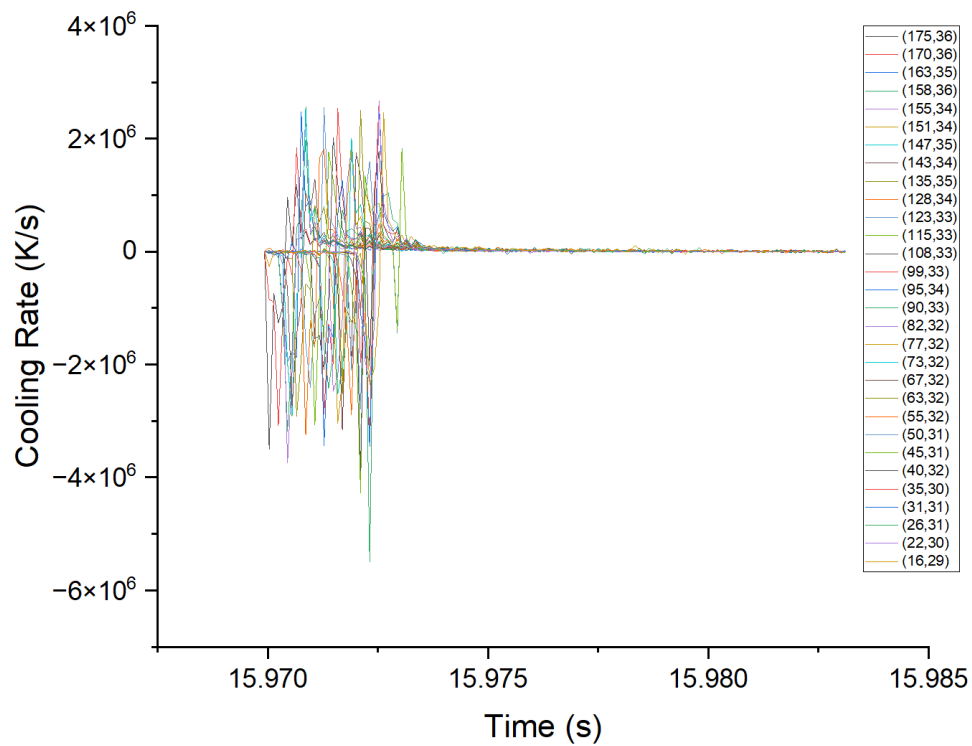


Figure 13. Cooling rate results of IR recording for the continuous scanning strategy in the fourth layer.

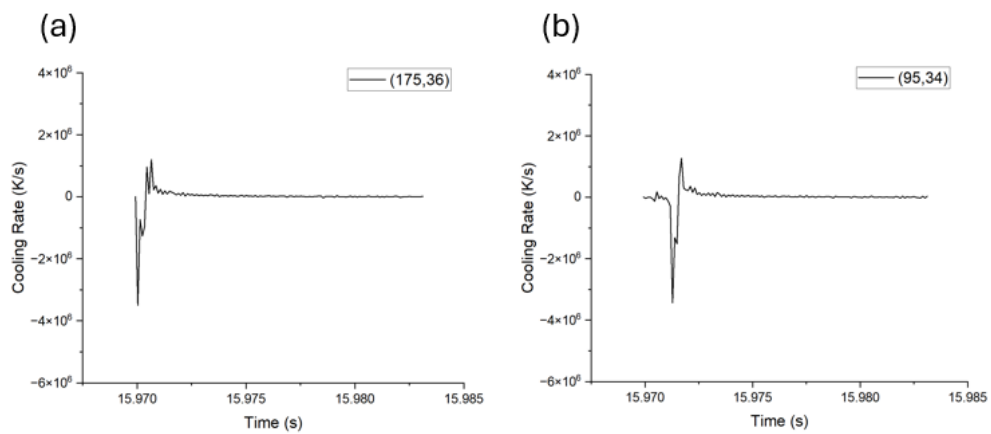


Figure 14. Cooling rate results of IR recording for the continuous scanning strategy in the fourth layer: (a) start point, (b) midpoint.

By comparison, discrete welding produces multiple periodic cooling pulses, where each laser spot generates a localized molten pool that cools rapidly, as shown in Figures 15 and 16. For both D3 and D4, the peak cooling rates consistently remain between  $6 \times 10^6$  and  $7 \times 10^6$  K/s, indicating strong potential for amorphous phase formation. Unlike continuous welding, the cooling rate trends across different positions within the same layer under discrete welding are highly consistent and show no decrease as scanning progresses. This stable behavior is primarily attributed to localized heat input, sufficient cooling intervals, and the maintenance of vertical thermal gradients, which ensure good thermal isolation and temporal separation between layers.

From an interlayer perspective, the continuous welding clearly shows a progressive reduction in cooling efficiency from the third to the fourth layer, evidenced by declining peak cooling rates and more pronounced drops toward the end of the scan path. This indicates deteriorating heat dissipation efficiency and increased thermal accumulation with each successive layer. In contrast, discrete welding demonstrates highly consistent and repeatable cooling behavior across layers, with no significant impact from increased layer count or changes in the scanning position, highlighting its superior thermal control and interlayer stability.

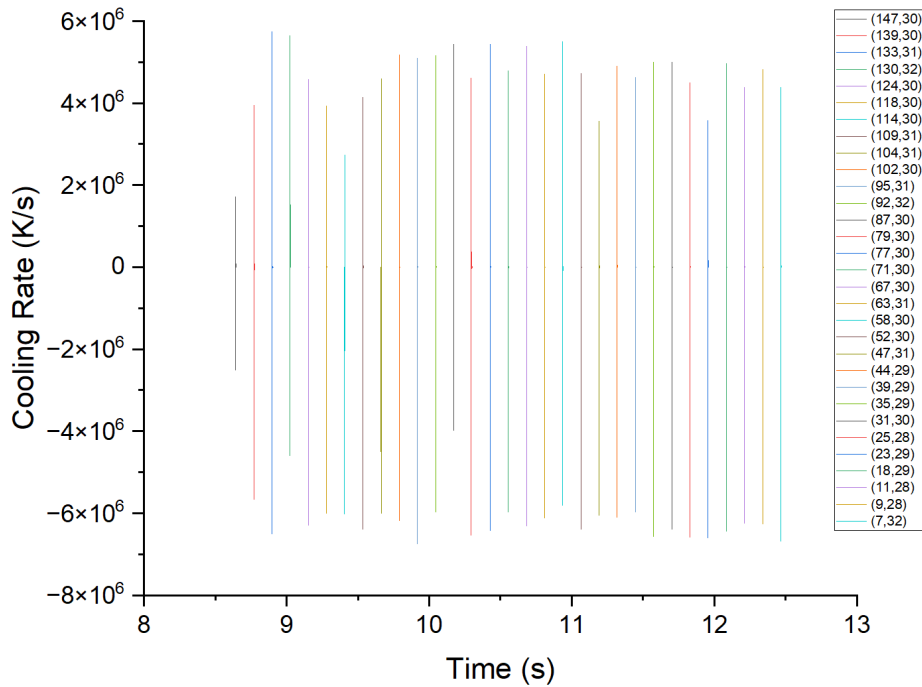


Figure 15. Cooling rate results of IR recording for the discrete scanning strategy in the third layer.

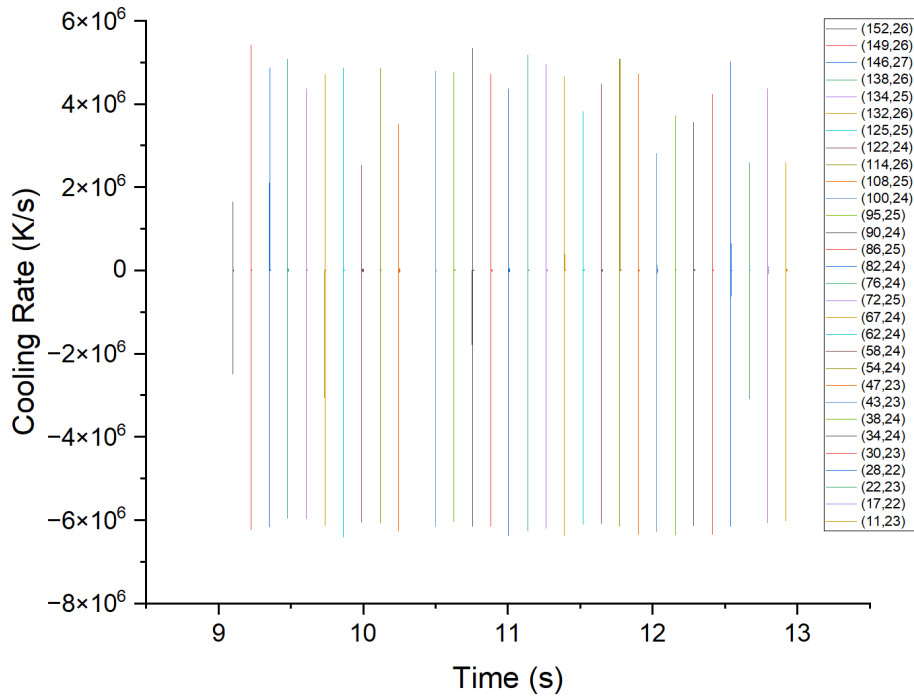


Figure 16. Cooling rate results of IR recording for the discrete scanning strategy in the fourth layer.

Overall, discrete welding outperforms continuous welding in cooling rate management, maintaining strong spatial thermal gradients and effective thermal isolation between layers. These characteristics ensure that sufficiently high cooling rates are achieved, fulfilling the requirement for fabricating metallic glasses.

### 3-3. Material Characterization of BMG

The XRD analysis clearly reveals that different scanning strategies and layer positions significantly affect the resulting material structure. In the third-layer samples, both the continuous scanning strategy and the discrete scanning strategy exhibit distinct crystalline diffraction peaks, as shown in Figures 17(a) and 17(c). These phases likely originated from elemental diffusion from the substrate or surface contamination during the laser processing, indicating partial crystallization in the third layer.

In contrast, the fourth-layer samples display broad amorphous humps without sharp diffraction peaks, confirming that a fully amorphous structure was retained, as shown in Figures 17(b) and 17(d). By integrating the temperature history and cooling

rate analysis, it can be inferred that the amorphous stability of the fourth layer is attributed to its increased distance from the substrate, improved vertical thermal insulation, and the maintenance of effective cooling rates, all of which help suppress thermally induced crystal nucleation.

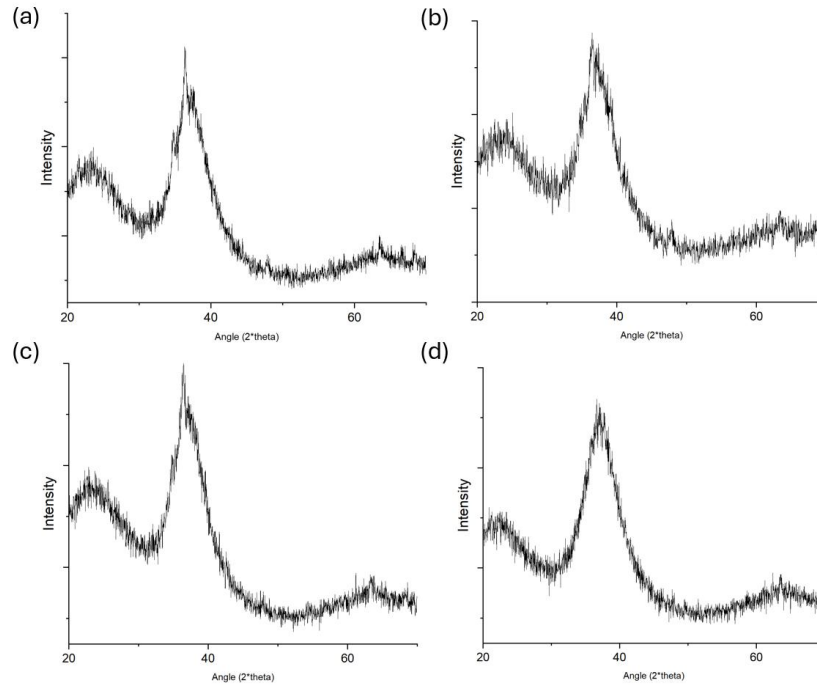


Figure 17. XRD results of (a) continuous scanning strategy in the third layer, (b) continuous scanning strategy in the fourth layer, (c) discrete scanning strategy in the third layer, and (d) discrete scanning strategy in the fourth layer

Notably, although the continuous welding in the fourth layer (C4) exhibits an overall lower cooling rate compared to the third layer (C3), its XRD pattern still shows a fully amorphous structure without any crystalline peaks. This seemingly contradictory observation can be explained by several interacting mechanisms as described below.

First, being farther from the substrate, the fourth layer is less affected by thermal diffusion and elemental contamination, thereby limiting the presence of heterogeneous nucleation sites and facilitating the preservation of the amorphous phase.

Second, although the cooling rate in C4 is reduced, it may still exceed the critical cooling rate (CCR) required for metallic glass formation. According to the literature, the CCR for LM105 is estimated to be around  $10^5$ – $10^6$  K/s. In this study, the cooling

rate in C4 was found to be within the range of  $7 \times 10^5$  to  $4 \times 10^6$  K/s, which is sufficient to suppress crystallization.

In summary, although the cooling rate in C4 is lower than in C3, the reduced contamination and nucleation tendency, combined with a still-effective cooling rate above the CCR threshold, contributes to the formation and retention of a stable amorphous structure.

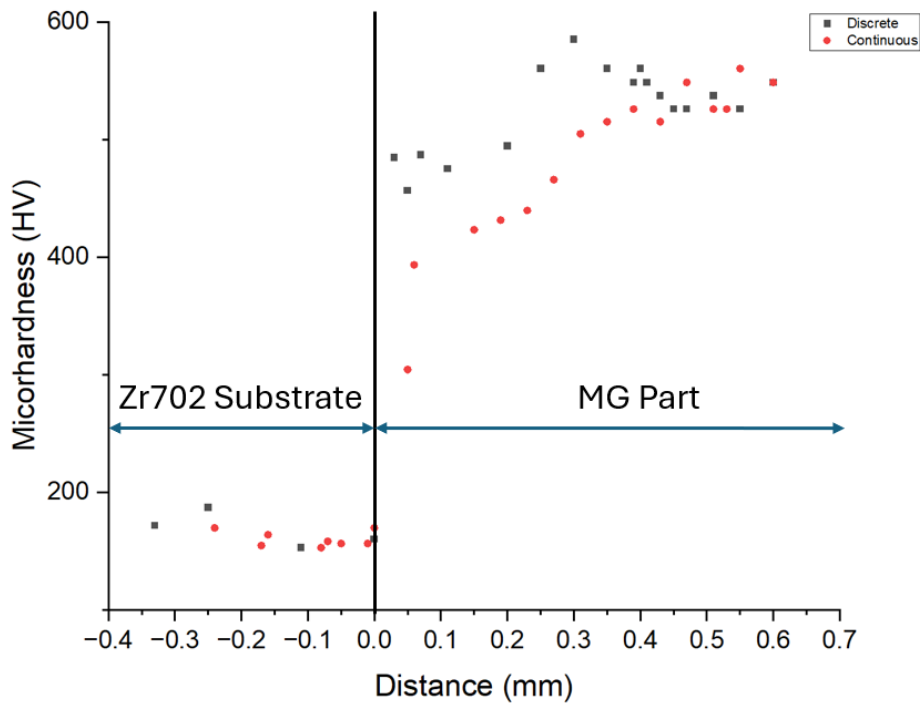


Figure 18. Microhardness of LFP-fabricated BMG parts

To investigate the influence of different scanning strategies the mechanical properties of the final built layers, microhardness tests were conducted on metallic glass samples fabricated using the continuous and discrete welding strategies, and the results were compared with the Zr702 substrate, as shown in Figure 18. The measurement results indicate that the average hardness of the Zr702 substrate was 162.74 HV, which is significantly lower than that of the laser-processed metallic glass region, demonstrating a substantial change in material properties after processing.

In the metallic glass region, both discrete and continuous welding samples exhibited significantly increased hardness. Statistical analysis shows that the average microhardness of the discrete welding samples reached 527.15 HV, higher than the

475.19 HV observed in the continuous welding samples. The overall trend indicates that discrete welding consistently achieved higher hardness values across most regions, with a maximum value of 585.3 HV. Compared to continuous welding, discrete welding demonstrates superior hardness performance.

Although XRD analysis confirms that both strategies retained a fully amorphous structure in the fourth layer, with no evidence of crystallization, the difference in hardness values suggests that even with identical phase compositions, factors such as microstructure or internal defects can still influence hardness. This phenomenon can be attributed to the intermittent heating and natural cooling characteristics of the discrete welding strategy, which effectively reduces heat accumulation, increases local cooling rates, and promotes the formation of a more stable amorphous structure. In contrast, the continuous energy input in continuous welding lowers cooling efficiency and leads to regional heat accumulation and thermal deformation, ultimately reducing the overall hardness performance.

#### **4. Conclusion**

This study systematically evaluated the thermal behavior, structural characteristics, and mechanical properties of metallic glass samples fabricated by Laser Foil Printing using two different laser scanning strategies: continuous welding and discrete welding. Through in-situ thermographic monitoring and subsequent material characterization, the study clearly revealed significant differences between the two strategies.

In continuous welding, the sustained laser energy input led to progressive heat accumulation in the upper layers, resulting in prolonged thermal exposure and an expanded heat-affected zone. This reduced cooling efficiency, particularly toward the end of the scan path, where the cooling rate gradually decreased. Although the cooling rate in the fourth layer remained above the critical cooling rate of the metallic glass, allowing to successfully preserve an amorphous structure, the resulting microhardness was still lower than that of the discrete welding samples.

In contrast, discrete welding generated sharp, localized thermal pulses, characterized by consistently high cooling rates, minimal heat accumulation, and strong thermal gradient control. These conditions effectively minimized the extent of the heat-affected zone and favored the retention of the amorphous phase. Correspondingly, the microhardness values achieved in discrete welding samples were superior.

Although both strategies can form amorphous structures in the top layers, discrete welding demonstrates superior performance in terms of thermal control and mechanical properties. These findings highlight the critical role of laser scanning strategy in optimizing the quality and functionality of metallic glass produced by LFP additive manufacturing.

## 5. Reference

- [1] Sohrabi, N., Jhabvala, J., & Loge, R. E. (2021). Additive manufacturing of bulk metallic glasses—process, challenges and properties: a review. *Metals*, *11*(8), 1279.
- [2] Khmyrov, R. S., Korotkov, A., Gridnev, M., Podrabinnik, P., Tarasova, T. V., & Gusarov, A. V. (2024). Phase Composition, Microstructure and Mechanical Properties of Zr<sub>57</sub>Cu<sub>15</sub>Ni<sub>10</sub>Nb<sub>5</sub> Alloy Obtained by Selective Laser Melting. *Journal of Manufacturing and Materials Processing*, *8*(1), 10.
- [3] Shen, Y., Li, Y., Chen, C., & Tsai, H. L. (2017). 3D printing of large, complex metallic glass structures. *Materials & Design*, *117*, 213-222.
- [4] Li, Y., Shen, Y., Leu, M. C., & Tsai, H. L. (2019). Mechanical properties of Zr-based bulk metallic glass parts fabricated by laser-foil-printing additive manufacturing. *Materials Science and Engineering: A*, *743*, 404-411.
- [5] Shen, Y., Li, Y., & Tsai, H. L. (2018). Evolution of crystalline phase during laser processing of Zr-based metallic glass. *Journal of Non-Crystalline Solids*, *481*, 299-305.
- [6] Li, Y., Shen, Y., Chen, C., Leu, M. C., & Tsai, H. L. (2017). Building metallic glass structures on crystalline metal substrates by laser-foil-printing additive manufacturing. *Journal of Materials Processing Technology*, *248*, 249-261.
- [7] Wang, Y. X., Zhao, Z. J., Chiang, H. C., & Hung, C. H. (2024). Fabrication of Zr-based Bulk Metallic Glass from Crystalline Foil Using Laser Foil Printing Process.
- [8] Everton, S. K., Hirsch, M., Stravroulakis, P., Leach, R. K., & Clare, A. T. (2016). Review of in-situ process monitoring and in-situ metrology for metal additive manufacturing. *Materials & Design*, *95*, 431-445.
- [9] Turk, T., Liu, T., Hung, C. H., Billo, R., Park, J., & Leu, M. C. (2025). In-situ thermographic monitoring and numerical simulations of laser-foil-printing additive manufacturing. *Virtual and Physical Prototyping*, *20*(1), e2440609.